Ultrasonic tracking of shear waves using a particle filter

Q1 Atul Ingle[a)]
Department of Electrical and Computer Engineering, University of Wisconsin-Madison, Madison, Wisconsin 53705 and Department of Medical Physics, University of Wisconsin-Madison, Madison, Wisconsin 53705

Chi Ma[b),c)]
Department of Medical Physics, University of Wisconsin-Madison, Madison, Wisconsin 53705

Tomy Varghese[d)]
Department of Medical Physics, University of Wisconsin-Madison, Madison, Wisconsin 53705 and Department of Electrical and Computer Engineering, University of Wisconsin-Madison, Madison, Wisconsin 53705

(Received 6 February 2014; revised 17 August 2015; accepted for publication 10 October 2015; published XX XX XXXX)

Purpose: This paper discusses an application of particle filtering for estimating shear wave velocity in tissue using ultrasound elastography data. Shear wave velocity estimates are of significant clinical value as they help differentiate stiffer areas from softer areas which is an indicator of potential pathology.
Methods: Radio-frequency ultrasound echo signals are used for tracking axial displacements and obtaining the time-to-peak displacement at different lateral locations. These time-to-peak data are usually very noisy and cannot be used directly for computing velocity. In this paper, the denoising problem is tackled using a hidden Markov model with the hidden states being the unknown (noiseless) time-to-peak values. A particle filter is then used for smoothing out the time-to-peak curve to obtain a fit that is optimal in a minimum mean squared error sense.
Results: Simulation results from synthetic data and finite element modeling suggest that the particle filter provides lower mean squared reconstruction error with smaller variance as compared to standard filtering methods, while preserving sharp boundary detail. Results from phantom experiments show that the shear wave velocity estimates in the stiff regions of the phantoms were within 20% of those obtained from a commercial ultrasound scanner and agree with the estimates obtained using a standard method using least-squares fit. Estimates of area obtained from the particle filtered shear wave velocity maps were within 10% of those obtained from B-mode ultrasound images.
Conclusions: The particle filtering approach can be used for producing visually appealing SWV reconstructions by effectively delineating various areas of the phantom with good image quality properties comparable to existing techniques.
[http://dx.doi.org/10.1118/1.4934372]

Key words: ultrasound, shear wave elastography, electrode vibration elastrography, particle filter

1. INTRODUCTION

The major goal of shear wave elastography is to distinguish between various tissue structures based on local variations in stiffness. With the assumption that tissues are elastic and incompressible and ignoring any high frequency dispersive effects, it is possible to relate shear wave velocity (c_s) and the elastic shear modulus (G) via the relation

$$c_s = \sqrt{\frac{G}{\rho}}, \tag{1}$$

where ρ is the density of the medium. Ignoring the effects of viscosity, c_s remains constant as a function of frequency. It is also worth noting that the Young's modulus (E) of an incompressible elastic material whose Poisson's ratio is close to 0.5 is related to its shear modulus by

$$G \approx E/3. \tag{2}$$

In ultrasound shear wave elastography, the shear modulus of the underlying tissue is estimated using ultrasound echo data acquired at high frame rates (usually with plane wave insonifications) on a clinical scanner. Various methods can be used for generating shear wave displacements in tissue—the most common ones being acoustic radiation force[1,2] Q2 and external mechanical excitation such as an actuator.[3–6] There are potentially unlimited configurations and methods for generating shear waves using mechanical excitation depending on the apparatus and the clinical application. In this paper, electrode vibration[5,6] is used for inducing shear waves with the target application being real-time monitoring of tumor ablation in the liver. This technique is called electrode vibration elastography (EVE). An advantage of EVE in monitoring liver ablation is that shear waves can be generated *in vivo* by vibrating the same radio-frequency (RF) electrode or microwave antenna that is being used for the ablation procedure. Compared to acoustic radiation force type techniques, electrode vibration can be used to obtain larger vibration amplitudes that can be tracked over longer distances in tissue.

The next step in shear wave elastography involves tracking these shear wavefronts in the underlying medium using ultrasound displacement estimation techniques. It is possible to calculate SWV by directly inverting the wave equation.[3,4,7] This method involves calculation of second order temporal and spatial derivatives of displacement estimates obtained from any standard ultrasound-based motion tracking algorithm. However, this method is fraught with noise, notwithstanding the use of standard noise reduction techniques such as median filtering for removing outliers and mean filtering for smoothing.

Alternatively, the location of these shear wavefronts as a function of time can be used for estimating SWV and hence the shear modulus using Eq. (1). For tissue-mimicking (TM) phantom experiments, the density is assumed to be equal to that of water (1000 kg/m^3). As is the case with most ultrasound based systems, presence of noise and outliers in raw ultrasound data must be mitigated to attain sufficient signal-to-noise ratios (SNRs) necessary for successful clinical application of this method. This paper gets to the crux of this issue by proposing a model-based denoising algorithm for SWV reconstruction from noisy ultrasound displacement data. The propagating shear wave consists of a single pulse which is tracked through the imaging plane by recording the time taken for the peak of this pulse to reach different lateral locations. This process is repeated at different depths in the imaging plane. These data are referred to as time-to-peak (TTP)[2] or time-of-flight data.[8]

Zheng *et al.*[9] apply harmonic excitation of a known frequency to produce a sinusoidal displacement shear wave in the medium of interest using ultrasound radiation force. The phase of this sinusoidal motion is detected using a similar principle as Doppler ultrasound and SWV is estimated from this phase information. A Kalman filter is used for obtaining optimum phase estimates from noisy ultrasound echo data. As opposed to the method of tracking small shear wave pulses, this method uses continuous sinusoidal excitation which allows characterization of the SWV as a function of frequency. Replicating this method for shear waves traveling through disparate media can be difficult as the vibrations are extremely small and may fall below the noise floor when traveling through interfaces.

McLaughlin and Renzi[10] use a correlation based pattern matching method to locate a shear wave pulse of a known shape at different locations in the medium. The issue of noise smoothing is handled implicitly by use of the Eikonal equation thereby avoiding derivatives of noisy data and circumventing the issue of solving an ill-posed inverse problem. In order to account for the phenomenon of pulse shape broadening, a penalized optimization procedure with an improved cross correlation based method for estimation of arrival times was used in a breast elastography application by Tanter *et al.*[11] and also in another recent paper by Klein *et al.*[12]

Various function fitting and denoising methods have been applied to the problem of filtering noisy TTP information. Palmeri *et al.*[2] apply linear regression followed by statistical goodness of fit criteria. Wang *et al.*[8] apply the random sample consensus (RANSAC) algorithm to address the issue of outliers. They model the TTP curve as a linear function of the spatial coordinates with the coefficients as free parameters to be estimated. The RANSAC algorithm proceeds by randomly drawing subsets of the full dataset. Next, it calculates the parameters of the hypothesized linear model using a least-squares (LS) fit and then identifies and removes possible outliers at each iteration.

Rouze *et al.*[13] proposed using the radon sum transform for estimating SWV in a single medium. Using a 3D map of lateral location, time, and displacement, the algorithm extracts a trajectory in the lateral location vs time plane that gives the maximum sum of displacements. This trajectory is assumed to be the path of propagation of the shear wave. Intuitively, this method gives the best fit line along the locations of the displacement peaks thereby smoothing out the effect of noise. Zhao *et al.*[14] analyze the effect of ultrasound imaging system parameters such as transducer type, frequency, and imaging depth on SWV estimates obtained using acoustic radiation force. A least-squares fit is used for the TTP data to estimate SWVs.

In a preliminary study, Bharat and Varghese[5] discuss the phenomenon of change in the slope of the TTP profile when a shear wave travels through an interface between different media. A least-squares fit is applied to the noisy TTP data prior to calculating the slope of the curve at various lateral locations for estimating SWV and locating any slope change points. It is important to develop algorithms to automatically and reliably detect these slope change locations of the TTP curve as they are indicators of the presence of a transition boundary between regions of different stiffness. The present work is an attempt in that direction.

A theoretical analysis of the complete signal processing chain employed in a standard ultrasound based SWV imaging system was presented in a paper by Deffieux *et al.*[15] Using methods from classical estimation theory, they derive a Cramér–Rao lower bound on the variance of any unbiased estimator of shear modulus when the shear wave propagates in a homogeneous linearly elastic medium with no interfaces. Tracking the propagation of a shear wavefront through multiple media is more challenging due to uncertainty regarding wave velocities within different media and exact locations of interfaces. As a result, direct application of statistical function fitting techniques provides no theoretical guarantees on detecting the interfaces and slopes accurately. From the point of view of TTP data, this problem is equivalent to fitting a continuous piecewise linear function with unknown slopes, unknown breakpoints, and unknown number of segments. This paper attempts to fill in this missing piece in algorithm development for tracking of shear waves propagating via multiple interfaces.

As opposed to *ad hoc* application of function fitting and smoothing techniques, the algorithm presented here first models the TTP data for a shear wave pulse propagating through multiple interfaces and then uses a stochastic filtering technique called the particle filter to estimate the SWVs that best fit the model.

2. THEORY AND ALGORITHM

2.A. Stochastic hidden Markov model

A shear wave can be assumed to travel with a constant speed as long as it propagates in the same homogeneous medium, but the speed changes when it enters a dissimilar medium via an interface. Therefore, to a first approximation, an ideal TTP curve should appear to grow linearly with a constant slope, except at interfaces, where the slope should abruptly change to a new value. Under this model, the slopes of individual segments in the noiseless TTP data can be used for obtaining SWVs in the respective media and the locations of joint points can be used to identify boundaries between dissimilar materials. Ultrasound imaging at high frame rate can be used for tracking axial tissue displacements as a function of time from which the TTP can be computed for various lateral locations. These signal processing steps leading up to the TTP estimates introduce some noise, which will be assumed to have a Gaussian distribution. A stochastic hidden Markov model can be formulated to represent the physical phenomenon of the traveling shear wave together with this noisy TTP measurement.

The following notation is used to describe the hidden Markov model. Let

- Z_n be the actual (noiseless) value of the TTP curve at a lateral location n,
- Y_n be the noisy measured value of the TTP curve,
- W_n be i.i.d. Gaussian noise with density $\mathcal{N}(0,\sigma^2)$,
- S_n be the most recent slope value of the curve,
- X_n be a continuous valued uniformly distributed random variable,
- M_n be a 2D "state variable," (Z_n,S_n),
- B_n be a Bernoulli random variable with $P(B_n=0)=p$ and $P(B_n=1)=1-p$ for some $0<p<1$.

Individual components of a vector are denoted using superscripts. For instance, $\mathbf{R}^{(l)}$ is used to denote the lth component of a vector $\mathbf{R}$. The shorthand notation $\mathbf{R}_{l:l+m}$ is used to denote the set of vectors $\{\mathbf{R}_l,\mathbf{R}_{l+1},\ldots,\mathbf{R}_{l+m}\}$. It is assumed that the TTP data are obtained at equally spaced sampling points along the lateral dimension. Hence, it is possible to normalize the distances to 1 unit/sample.

The relationship between these random variables can now be summarized as follows:

$$Z_{n+1} = Z_n + S_n, \tag{3}$$

where

$$S_{n+1} = \begin{cases} S_n & \text{if } B_n = 0 \\ X_n & \text{if } B_n = 1 \end{cases}$$

and

$$Y_{n+1} = Z_{n+1} + W_{n+1}. \tag{4}$$

These equations model the presence of interfaces in a probabilistic manner. At any lateral location, the shear wave continues to propagate in the same medium with a probability p or encounters an interface with a probability $1-p$ and the slope switches to a new values chosen uniformly randomly over some reasonable interval $[LB,\ UB]$. In most practical scenarios, the value of p can be chosen to be close to 1 because one expects to propagate through very few interfaces.

This hidden Markov model that generates the noisy TTP data can be cast into this standard form with a "state evolution equation" given by

$$M_{n+1} = \begin{bmatrix} M_n^{(1)} + M_n^{(2)} \\ (1-B_n)M_n^{(2)} + B_n X_n \end{bmatrix} \tag{5}$$

and an "observation equation" given by

$$Y_n = M_n^{(1)} + W_n. \tag{6}$$

The dependence between various random variables involved in this model is pictorially represented in Fig. 1.

2.B. Particle filter

Particle filtering (PF) is a Monte Carlo technique that calculates the approximate probability density function of the state variables conditioned on observed data. This is achieved by traversing all the data points sequentially and updating the density estimate based on an application of Bayes' rule. Particle filtering methods have been applied in the context of quasistatic elastography[16] and for sequential tracking problems in medical imaging.[17,18] The present work is, to the best knowledge of the authors, the first time a particle filtering approach has been used for inverse problems in dynamic elastography. Detailed description of various embellishments in the basic algorithm and implementation issues are discussed in a tutorial article by Arulampalam *et al.*[19] Some practical implementation issues and simulation results with real world examples are discussed in the paper by Gilks and Berzuini.[20] Development of the theory behind optimality of particle filters for hidden state estimation when the noise distribution is not Gaussian can be found in the paper by Bergman *et al.*[21]

For the present problem, a particle filter is used to obtain maximum *a posteriori* estimates for the states $\{M_1,\ldots,M_N\}$

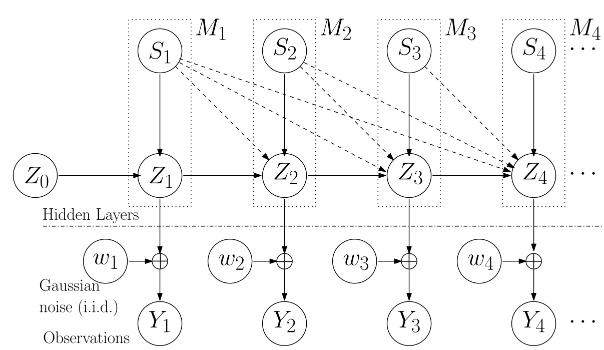

FIG. 1. A pictorial representation of the relationships between various random variables (input, hidden states, and output) of the hidden Markov model is shown here. Every hidden state M_n has two components, and the observed values Y_n are obtained after addition of i.i.d. zero mean Gaussian noise to the first component. The second component is the local slope value S_n which obeys a Markov structure. The slope stays constant with a probability p and changes to a new uniformly randomly chosen value with a probability $1-p$; the uniform random variable X_n acts as an input to the model.

conditioned on the data $\{Y_1,\ldots,Y_N\}$, where N is the number of data points. Suppose that the algorithm is at the kth data point out of the N available observations. The density of the current state conditioned on all data points observed so far can be expressed approximately as a weighted sum of Dirac-delta functions as

$$p(M_k|Y_{1:k}) \approx \sum_{i=1}^{N_s} \omega_k^i \delta(M_k - M_k^i), \tag{7}$$

where N_s is the number of points used in the discrete approximation, $\{M_k^i\}_{i=1}^{N_s}$ is a set of random points in the state space, and $\{\omega_k^i\}_{i=1}^{N_s}$ is a set of corresponding weights that sum to 1. The number of points N_s is typically quite large ($\sim 10^3$–10^4) so that the discrete approximation is close to the actual continuous density function.

For the Dirac-delta approximation to hold, each random point M_k^i must be drawn according to the density function $p(M_k|Y_{1:k})$. However, since this probability density function is unknown, a special technique of importance sampling[19,20] is used to generate these points. The points $\{M_{0:k}^i\}_{i=1}^{N_s}$ are generated using the sampling density $p(M_k^i|M_{k-1}^i)$ which leads to the weight update equation given by[19]

$$\omega_k^i = \omega_{k-1}^i p(Y_k|M_k^i). \tag{8}$$

Additionally, a procedure called "resampling" is used to generate a modified particle set in such a way that a majority of the sample points remain concentrated in high probability density regions. A regularized particle filter implementation is used in this paper where a random perturbation is added to each point after resampling. Under certain assumptions,[22] the optimal choice for these perturbations is the Epanechnikov kernel.[23]

The expected value of the current state can be obtained from the density estimate as

$$E[M_k|Y_{1:k}] = \sum_{i=1}^{N_s} \omega_k^i M_k^i. \tag{9}$$

Moreover, the variance of this estimate can also be calculated,

$$\mathrm{Var}[M_k|Y_{1:k}] = E[(M_k)^2|Y_{1:k}] - (E[M_k|Y_{1:k}])^2 \tag{10}$$

where the square is taken elementwise. This may be used in practice to show a "standard deviation image" along with a SWV map to give feedback on the reliability of the estimated SWVs and thus can be of clinical value.

Better smoothing estimates may be obtained if the observations from the future are also incorporated into the current state estimation step. This is done using a lookahead-window smoothing method that waits for L samples into the future before generating the current state estimate as

$$E[M_k|Y_{1:k+L}] = \sum_{i=1}^{N_s} \omega_{k+L}^i M_k^i. \tag{11}$$

Choosing L to be very large has pitfalls of oversmoothing[24] and wasting some data samples toward the end of the dataset. As a further improvement, Doucet *et al.* also propose the "fixed lag smoothing" algorithm[24] which runs a backward smoothing step to update the weights according to

$$\hat{\omega}_k^i = \sum_{j=1}^{N_s} \hat{\omega}_{k+1}^j \frac{\omega_k^i\, p(M_{k+1}^j|M_k^i)}{\sum_{l=1}^{N_s} \omega_k^l\, p(M_{k+1}^j|M_k^l)},$$

for $k = n-1,\ldots,1$ and $\hat{\omega}_n^i = \omega_n^i$. Note that this is computationally more burdensome to implement in real-time applications [because of the need to process and store N_s^2 different values of $p(M_{k+1}^j|M_k^l)$ at each k]. Therefore, this last equation is only used in evaluation of the HMM approach in simulations; the lookahead-window smoother is used for the experimental data.

The complete algorithm is presented in pseudocode style in the Appendix in Figs. 11–13.

3. MATERIALS AND METHODS

3.A. Design of ablation phantoms

The phantom based study involved data acquisition from two TM phantoms with similar design but slightly different mechanical properties.[25] Both phantoms consist of a centrally situated stiff ellipsoid in a softer background material which simulates the presence of a tumor in cirrhotic liver tissue. The stiff ellipsoid is intended to model an ablated region. An irregular tumor structure whose stiffness was in between the ablated region and the background material was attached on one side of the ellipsoid. The phantom material is composed of a dispersion of microscopic oil droplets in a gelatinous matrix. The difference in stiffness is mainly achieved by controlling the proportion of oil in the material; a detailed discussion about the design and properties of such phantom materials is given in the paper by Madsen *et al.*[26] A stainless steel rod was bonded to the center of the ellipsoid in order to mimic the role of a RF electrode or a microwave antenna in an actual ablation procedure. This rod was used for generating shear waves in the phantom with the help of an actuator. A representative cross-sectional view of the structure of both phantoms is shown in Fig. 2(a). The gelatin block was 14×14×9 cm. This block was placed in an open top 1 cm thick acrylic container. A layer of safflower oil about 2 cm deep was poured over the top surface to prevent desiccation.

3.B. Finite element simulation model

One image plane of a stiff ellipsoidal inclusion embedded in a soft background material was simulated using a finite element model in ANSYS. This is similar to the schematic shown in Fig. 2(a) without the irregularly shaped region. The Young's modulus of the inclusion was set at 55 kPa whereas that of the background was set at 5 kPa. Both materials were modeled to be perfectly linearly elastic and incompressible with no viscosity. The needle was modeled using a stainless steel rod firmly bonded to the ellipsoid, but free to slide along the surface adjoining the softer background material. More details about the model can be found in the paper by DeWall and Varghese.[6]

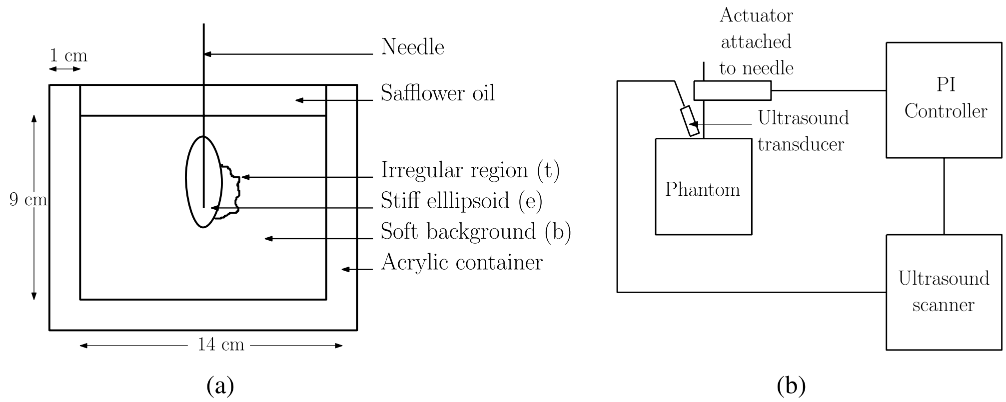

FIG. 2. A cross-sectional view (not to scale) of the two phantoms used for experimental validation is shown in (a). Both phantoms consist of a stiff ellipsoidal inclusion embedded in a softer background material. The stiff region mimics the presence of completely ablated tissue, whereas the softer background simulates unablated tissue. An irregularly shaped partially ablated region of intermediate stiffness is present on one side of the inclusion. A block diagram of the data acquisition system is shown in (b). The needle is vibrated in a single pulse motion using an actuator operated in synchronization with the ultrasound scanner. RF echo data are acquired from a linear array transducer.

3.C. Data acquisition system

Ultrasound RF echo data were acquired using an Ultrasonix SonixTouch machine (Ultrasonix Medical Corporation, Richmond, BC, Canada) and a software tool developed using the Ultrasonix software development kit.[6] The 9L4 linear array transducer operated at a frequency of 5 MHz was used for obtaining ultrasound RF echo data. Focussed transmit and receive were used with a 30 mm focal depth and 45 mm imaging depth for Phantom-1. An imaging depth of 50 mm was used for Phantom-2. The transducer had a 6 dB bandwidth of 33%, a transmit F-number of 2.6 and an acoustic pulse duration equal to 1 transmit cycle of the operating frequency of 5 MHz. The effective line density was equal to the number of elements, i.e., 128 lines over a lateral extent of 3.8 cm.

The shear wave pulse was tracked at five lateral locations along the face of the transducer to get an effective frame rate of 2070 Hz. Individual shear wave pulses were generated by vibrating the needle with a pulse shape of a half-sinusoid with 100 μm amplitude and 30 ms width. A single time-limited pulse vibration allows localization of the shear wave in space and time using the TTP approach. Pulses were generated once per second to allow perturbations from the previous pulse to decay to a negligible amplitude and hence avoid simultaneous interfering waves. The needle was vibrated using a piezoelectric actuator [Physik Instrumente (PI) GmbH, Karlsruhe, Germany] that was attached to the stainless steel rod as shown in Fig. 2(b). In order to synchronize data collection and pulse generation, the PI controller was set up to trigger the ultrasound scanner and the actuator simultaneously.

Additionally, SWV and Young's modulus data were acquired with a Supersonic Imagine Aixplorer scanner (Supersonic Imagine, Aix-en-Provence, France) which uses a proprietary radiation force technique termed supersonic shear imaging (SSI).[27]

Mechanical stress–strain testing can be used for direct estimation of material stiffness. Samples of various regions in the phantoms were tested using a Bose Enduratec ELF 3200 machine (Bose Corp., Eden Prairie, MN, USA). Each sample was a cylinder with a diameter of 2.6 cm and a thickness of 1.0 cm. The machine was programmed to apply an average compression of 2% in a low frequency (20 Hz) dynamic testing mode.

3.D. Data processing

3.D.1. Synthetic data

Synthetic ground truth data vectors consisting of 50 data points each were generated with the parameters $p = 0.85, 0.90, 0.95$ and X_n chosen uniformly randomly in the interval [0,1]. Gaussian i.i.d. noise with zero mean and variances $\sigma^2 = 0.01, 0.03, 0.06, 0.16, 0.40, 1.00$ was added to the data. The particle filtering algorithm with a backward smoothing step as described in Sec. 2.B was applied to 50 independently generated data vectors. The mean squared error (MSE) between the estimated slope values and true slope values was calculated for each vector using the formula $1/50\sum_{i=1}^{50}(\hat{S}_i - S_i)^2$, where $\hat{S}_i$ is the estimated slope at data point i and S_i is the ground truth slope value. For comparison, the same noisy data vectors were smoothed using two other methods: (a) 4th order polynomial fit, (b) 10 point moving average (MA) filter, (c) 10 point quadratic Savitzky–Golay filter, and (d) 15 point cubic Savitzky–Golay filter. The slopes were then estimated via finite differencing and MSE with respect to the ground truth was calculated using the same formula. The mean MSE and standard deviation were calculated by repeating this procedure on the 50 independent data vectors. The particle filter was run with parameters $N_s = 5000$, $N_T = 10$, and $[LB, UB] = [0,1]$. The p and σ^2 values were set equal to those used for generating the synthetic data.

3.D.2. Finite element simulation data

Displacement profiles as a function of time for each pixel in the image plane were exported from the finite element simulation results. I.i.d Gaussian noise was added to this ground truth data for a 20 dB SNR with respect to the peak displacement (vibration amplitude). The displacement vs time profiles were used to estimate TTP for each pixel. A frequency domain low pass filter was used to reliably locate the peak. The

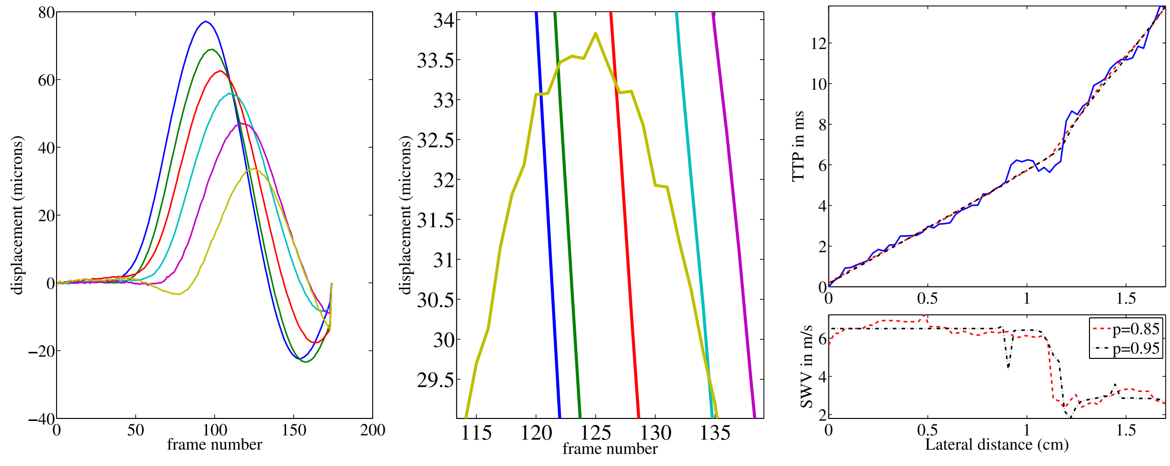

(a) (b) (c)

Fig. 3. Frame-to-frame displacements are obtained from the RF echo data and TTP is estimated from displacement vs time profiles for each pixel in the imaging plane. Displacement profiles for six different pixels using data from Phantom-1 are shown in (a). The six displacement plots correspond to pixels located at lateral distances from 0 to 1.8 cm in increments of 0.3 cm and at a depth of 3 cm. A zoomed section of the displacement profiles is shown in (b). This noise causes uncertainty in exact values of TTP which appears as noise in the TTP plot shown in (c). Two particle filter fits with $p = 0.85$ and $p = 0.95$ are also shown overlaid on the noisy TTP. Note that the smaller value of p results in more "jumps" in the final fit as seen from the SWV estimates. The TTP values and frame numbers are related via the imaging frame rate.

cutoff frequency of this low pass filter was chosen adaptively by discarding all frequency components that were smaller than 10% in magnitude compared to the largest component in the frequency spectrum. The location of the peak displacement was estimated with subframe-number resolution using a 5-point quadratic fit. The resulting TTP plots were analyzed along lines of constant depth on both sides of the needle using four different algorithms to estimate SWVs: (a) particle filter from Sec. 2.B, (b) 10 point moving average followed by finite differencing, (c) 10 point quadratic Savitzky–Golay differentiator, and (d) 15 point cubic Savitzky–Golay differentiator. The particle filter was run with parameters $N_s = 5000$, $N_T = 10$, and $[LB, UB] = [0,10]$, $p = 0.98$, and $\sigma^2 = 0.25$. The final SWV image was filtered with a 1×1 mm median filter.

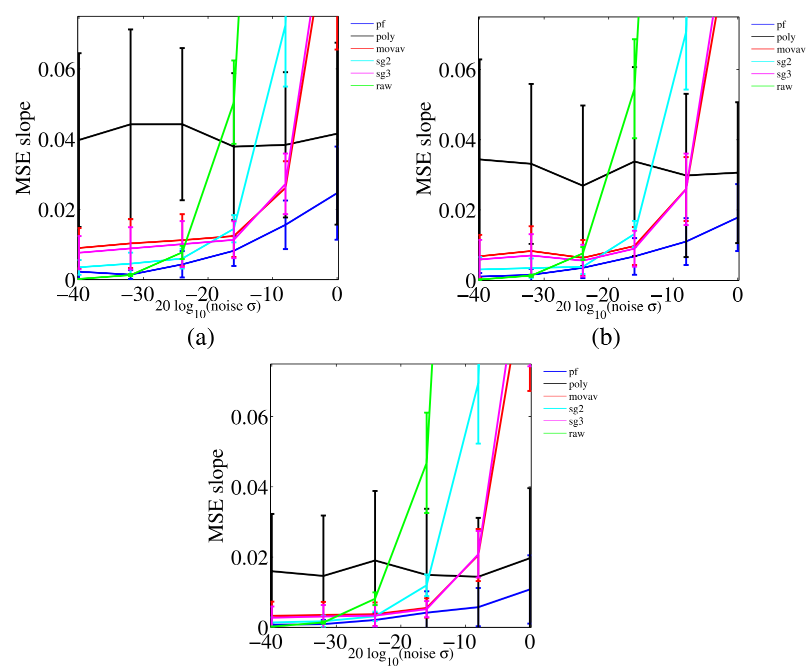

(c)

Fig. 4. MSE of estimated slope values from three different noise filtering methods applied to randomly generated piecewise linear data. Simulated piecewise linear data were filtered using three different filtering algorithms (pf = particle filter, poly = 4th order polynomial, movav = moving average 10 point window, sg2 = Savitzky–Golay quadratic with 10 point span, sg3 = Savitzky–Golay cubic with 15 point span, raw = no filtering). Local slope values were estimated by finite differencing. MSE from 50 independent simulated data vectors is presented in this figure. The particle filter provided the lowest mean MSE. (a) $p = 0.85$, (b) $p = 0.90$, and (c) $p = 0.95$.

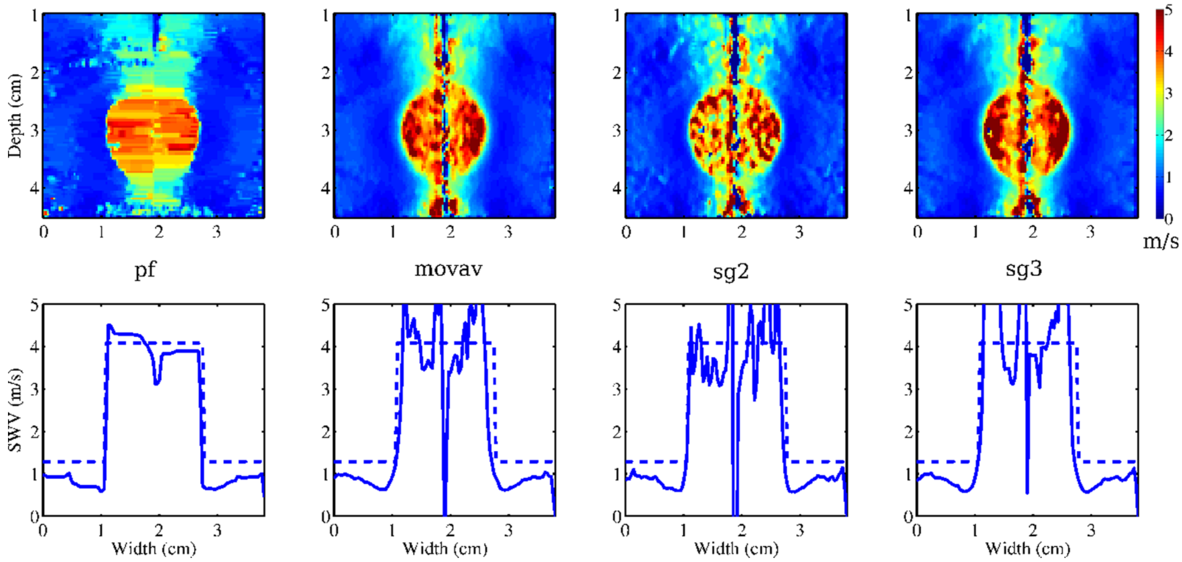

FIG. 5. SWV maps reconstructed from data obtained from the finite element simulation model are shown here. The top row shows images reconstructed using a particle filter with parameters $(p,\sigma^2) = (0.98, 0.25)$ (pf), moving average 10 point window (movav), Savitzky–Golay quadratic with 15 point span (sg2), and Savitzky–Golay cubic with 20 point span (sg3), respectively, from left to right. The bottom row shows SWV values along a horizontal line at a constant depth of 3 cm. True SWV profiles from the finite element model are shown with dotted lines.

The true SWV map was obtained from the finite element model by converting shear moduli to SWVs using Eq. (1). Finally, MSE values were calculated with respect to these true SWV values. MSE was estimated separately along each line of constant depth, on both sides of the needle.

3.D.3. Phantom experimental data

RF data obtained from the data acquisition system were used for tracking the lateral movement of the shear wave pulse at different depths. Axial displacement estimation was performed at each point in the imaging plane with the help of a cross correlation based displacement estimation algorithm.[28] Correlations were calculated along every corresponding A-line over successive frames of the RF data. 2 mm long windows with 75% overlap were used and the displacements thus obtained were accumulated over the entire duration of the acquired RF frames. This provided a displacement vs time profile for each pixel in the imaging plane. The noise term W_n in the Markov model subsumes all sources of noise that cause uncertainty in the measured TTP values. The uncertainty may arise from electronic noise in the RF echo data, uncertainties from the displacement estimation routine, and errors in finding the peak of the displacement profiles as shown in Fig. 3. The TTP for each location of interest was obtained using the same low pass filtering and peak finding algorithm as that used for the finite element simulated data. In general, reflections from interfaces between media of different stiffnesses may cause secondary reflected shear wavefronts. These can be suppressed using a spatiotemporal directional filter.[29,30] However in the present setup, reflection artifacts did not cause a problem because the shear wave pulse travels from a stiff medium into a softer medium.

TTP data were obtained as a function of lateral distance away from the needle at various depths in the phantom. The noisy TTP data were then filtered using two different methods. In the first method, the particle filtering algorithm discussed in Sec. 2.B was used, the second method used a least-squares fourth-order polynomial fit, and the third method uses a 10 point moving average filter. The particle filter was run with parameters $N_s = 5000$, $N_T = 10$, $[LB, UB] = [0,10]$, $p = 0.98$, and $\sigma^2 = 0.25$. The reciprocal of the slope of this TTP curve was used to estimate the SWV at different lateral locations and generate a SWV map. The image was finally smoothed using

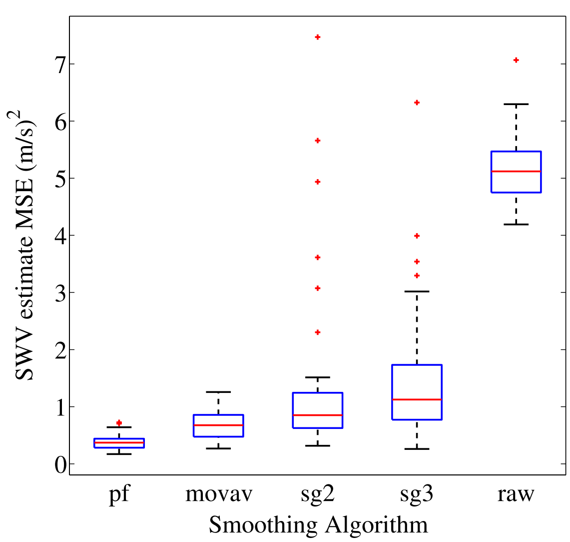

FIG. 6. A finite element simulation model was used to export frame-to-frame displacements which were processed using various algorithms to estimate SWV. Mean squared reconstruction error in the SWV maps produced from the finite element simulation model is shown here, where the SWV from the finite element model was used as ground truth. (pf = particle filter, movav = moving average 10 point window, sg2 = Savitzky–Golay quadratic with 15 point span, sg3 = Savitzky–Golay cubic with 20 point span, raw = no filtering.)

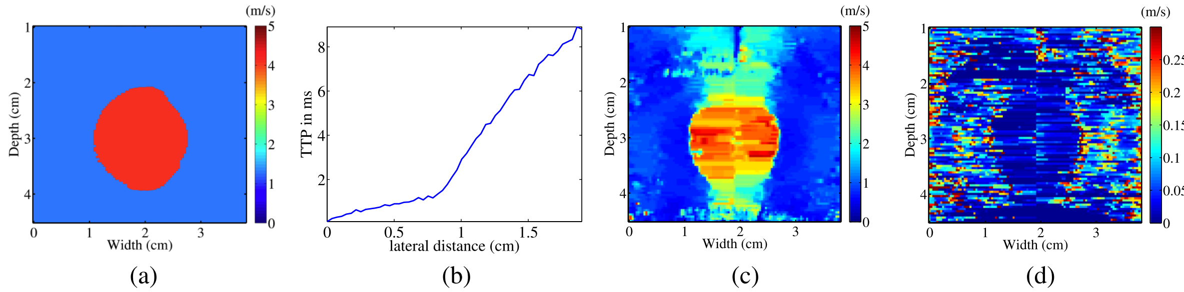

FIG. 7. The ideal SWV image from the finite element model is shown in (a). The ground truth SWV values are 4.28 and 1.28 m/s in the inclusion and the background, respectively. A representative TTP plot along a line at a depth of 3 cm to the right of the needle is shown in (b). The SWV image shown in (c) is generated by processing these TTP curves at all depths using the particle filter. Since the SWV values are obtained using a Bayesian model, the posterior density can be used to produce a standard deviation image that provides feedback about the reliability of the SWV estimates. The standard deviation image in (d) is calculated using the square root of the quantity in Eq. (10) for each pixel in the SWV image.

a 1×1 mm median filter[6] to remove outliers and suppress any linear streak artifacts that appear from processing individual lines at constant depth.

Various statistics such as SNR,[31] contrast (C), and contrast to noise ratio (CNR)[32] were calculated from the SWV maps over three different ROIs each of size 10×5 mm. The three ROIs were located in the stiff inclusion, the irregular tumor, and the background region, respectively.

The following performance metrics were calculated from the ROIs fixed in the three regions of the phantoms. The locations of these ROIs are indicated in Figs. 8 and 9. For each region, the SNR is defined as

$$\mathrm{SNR} = \frac{\mu}{\sigma},$$

where μ and σ, respectively, denote the mean and the standard deviation values of the SWVs calculated over the ROI. The contrast (C) between a pair of regions is defined as

$$C = \frac{\mu_1}{\mu_2}$$

where the subscripts indicate two different media. Similarly, the contrast to noise ratio (CNR) is defined as[32]

$$\mathrm{CNR} = \frac{2(\mu_1-\mu_2)^2}{\sigma_1^2+\sigma_2^2}.$$

Besides mechanical properties, accurate estimation of the area of a stiff ablated region is also of clinical significance because radiologists are interested in ablating the right volume of cancerous tissue, along with a safety margin around the tumor. Area estimates were obtained by manually outlining the inclusion boundary in the SWV images obtained using particle filtering, least-squares polynomial fitting, and B-mode ultrasound.

4. RESULTS

4.A. Simulation results with synthetic data

This section discusses simulation results involving synthetic piecewise linear data. The results shown in Fig. 4 show that the particle filter outperforms four other smoothing methods considered. It is not surprising that finite differencing of the raw noisy data without any smoothing has the largest MSE as seen in the three insets.

Note that for any constant value of p, the particle filter outperforms other filtering methods at all noise levels. It is also worth noting that the performance gap gradually decreases as p increases from 0.85 to 0.95. This is because at larger values of p there are fewer change points in the piecewise linear function (on average) and so the filtering problem is "easier" in the sense that it only has one or two straight line segments.

In practice, the parameters p and σ^2 and the upper and lower limits of the uniform distribution are not known in advance. One way to bypass problem is by estimating these values from the raw data and using these estimates as inputs to the particle filtering algorithm. The value of p is set based on the ratio of the expected number of interfaces in the physical experiment to the number of points in the dataset. The sample variance of the raw data is used as an estimate for σ^2. The lower limit for the distribution of X_n can be set to any small

TABLE I. Shear wave velocity estimates.

		Phantom-1			Phantom-2		
		e	t	b	e	t	b
	SWV PF (m/s)	3.07 ± 0.7	2.02 ± 0.32	0.91 ± 0.31	4.68 ± 1.3	2.99 ± 0.4	1.32 ± 0.68
EVE	SWV LS (m/s)	3.14 ± 0.79	1.96 ± 0.23	1.16 ± 0.12	4.56 ± 0.75	3.1 ± 0.32	2.09 ± 0.2
	SWV MA (m/s)	2.97 ± 0.75	1.57 ± 0.24	0.96 ± 0.18	4.66 ± 2.3	2.46 ± 0.3	1.74 ± 0.39
SSI	SWV (m/s)	2.8 ± 1.1	2.3 ± 0.8	1.3 ± 0.4	4.1 ± 1.8	2.4 ± 1.4	2.1 ± 0.7

Note: Values of SWV of different regions in the two phantoms obtained from PF, LS filtering, and MA filtering applied to the TTP data. Corresponding values obtained from the Supersonic Imagine scanner are also indicated. (e = ellipsoidal inclusion, t = irregular tumor region, b = background.)

TABLE II. Young's modulus estimates.

		Phantom-1			Phantom-2		
		e	*t*	*b*	*e*	*t*	*b*
EVE	*E* PF (kPa)	29.6 ± 13	12.6 ± 3.8	2.74 ± 1.5	70.6 ± 52	27.3 ± 6.9	6.62 ± 9.5
	E LS (kPa)	31.5 ± 18	11.7 ± 2.7	4.07 ± 0.86	63.9 ± 21	29.2 ± 6	13.2 ± 2.4
	E MA (kPa)	28.2 ± 14	7.61 ± 2.5	2.87 ± 1.2	NA[a]	18.4 ± 4.4	9.52 ± 4.8
SSI	*E* (kPa)	24.2 ± 5.8	13.3 ± 3.5	4.8 ± 0.5	50.1 ± 10.5	17.6 ± 4.8	13.6 ± 1.6
ELF	*E* (kPa)	56.57 ± 0.25	24.74 ± 0.63	4.55 ± 0.06	41.05 ± 0.20	20.52 ± 0.54	15.10 ± 0.80

Note: Values of Young's modulus of different regions in the two phantoms obtained from PF, LSs filtering and MA filtering applied to the TTP data. Corresponding values obtained from the Supersonic Imagine scanner and mechanical testing are also indicated. (*e* = ellipsoidal inclusion, *t* = irregular tumor region, *b* = background.)
[a]Variance of the estimate was too high to be useful.

positive number and a reasonable upper limit can be computed from the raw data. In practice, small errors in the input values of p and σ^2 did not affect the final fit drastically. However, it is crucial that the lower limit for the uniform distribution be set correctly. If this value is larger than the smallest slope in the data then the final fit would be just a straight line with a slope equal to the lower limit.

TABLE III. SNR, *C*, and CNR.

	Regions	Method	Phantom-1	Phantom 2
SNR (dB)	*e*	PF	13.2 ± 1.2	13.2 ± 3
		LS	12.4 ± 1.3	16.8 ± 2.7
		MA	12.8 ± 2.4	12.7 ± 4.6
	t	PF	16.6 ± 2	18.4 ± 2.5
		LS	19.8 ± 1.1	20.3 ± 1.2
		MA	17.8 ± 3.2	19.2 ± 1.1
	b	PF	9.67 ± 1.6	6 ± 1.8
		LS	20.6 ± 1.8	23.4 ± 1.7
		MA	17.8 ± 4.2	13.9 ± 2.1
C (dB)	*e*/*t*	PF	3.62 ± 0.56	3.83 ± 0.67
		LS	4.1 ± 0.6	3.39 ± 0.49
		MA	5.6 ± 0.66	5.66 ± 1.7
	t/*b*	PF	7.06 ± 0.8	7.15 ± 0.77
		LS	4.56 ± 0.6	3.5 ± 0.53
		MA	4.26 ± 1.1	2.97 ± 0.67
	e/*b*	PF	10.7 ± 0.7	11 ± 1
		LS	8.66 ± 0.6	6.89 ± 0.85
		MA	9.85 ± 0.7	8.62 ± 1.4
CNR (dB)	*e*/*t*	PF	11.8 ± 2.8	12.8 ± 3.7
		LS	13.1 ± 2.7	17.9 ± 4.2
		MA	17.5 ± 5	17.3 ± 6.3
	t/*b*	PF	22.9 ± 3.6	19.7 ± 2.7
		LS	27.5 ± 1.8	25.5 ± 1.9
		MA	20.3 ± 3.7	13.4 ± 5.6
	e/*b*	PF	24.6 ± 1.8	23 ± 4.1
		LS	22.6 ± 2.2	28.5 ± 5.1
		MA	24.5 ± 4.8	21.7 ± 7

Note: Values of SNR, *C*, and CNR obtained for various pairs of regions in the two phantoms using the three different algorithms. (PF = particle filter, LS = least squares, MA = moving average.) All numbers are in decibel. (*e* = ellipsoidal inclusion, *t* = irregular tumor region, *b* = background.)

4.B. Results from finite element simulation data

SWV images reconstructed from the finite element simulation data are shown in Fig. 5. Compared to other smoothing methods, the particle filter not only preserves the sharp boundary details but also provides a lower mean squared reconstruction error as seen from the representative SWV profiles shown along a line at a constant depth of 3 cm. The spike near the center column is an artifact due to the needle.

MSE values were obtained along lines of constant depth on both sides of the needle between the depths of 2.5 and 3.5 cm. The box plot in Fig. 6 shows a summary of these values for four different methods used for obtaining SWV images from the noisy TTP image. The SWV image corresponding to the stiffness distributions used in the finite element model was used as the ground truth for obtaining each MSE measurement. It can be seen that the particle filter provides the lowest median MSE with smallest spread among the methods considered.

Standard deviation of the estimated SWV values calculated using Eq. (10), SWV values can be displayed for the clinician alongside the SWV image as seen in Fig. 7. Note the stray high standard deviation pixels occur at locations laterally away from the needle where the shear wave pulse is more difficult to track due to decreased peak displacement. However, most of the pixels have variance close to zero indicating that the SWV estimate is reliable (assuming the Bayesian model is correct).

4.C. Experimental results from TM phantoms

Ten independent datasets were obtained from each of the two TM phantoms using the experimental setup described

TABLE IV. Inclusion area estimates.

Method	Phantom-1	Phantom-2
SWV PF	4.45 ± 0.15	4.13 ± 0.18
SWV LS	4.11 ± 0.19	4.01 ± 0.14
B-mode	4.68 ± 0.14	4.47 ± 0.11

Note: Estimates of area in square centimeter of the ellipsoidal inclusion obtained from the SWV maps and B-mode images are shown. Areas were estimated by manually outlining the inclusion and calculating the mean and standard deviation of the areas over ten independent datasets.

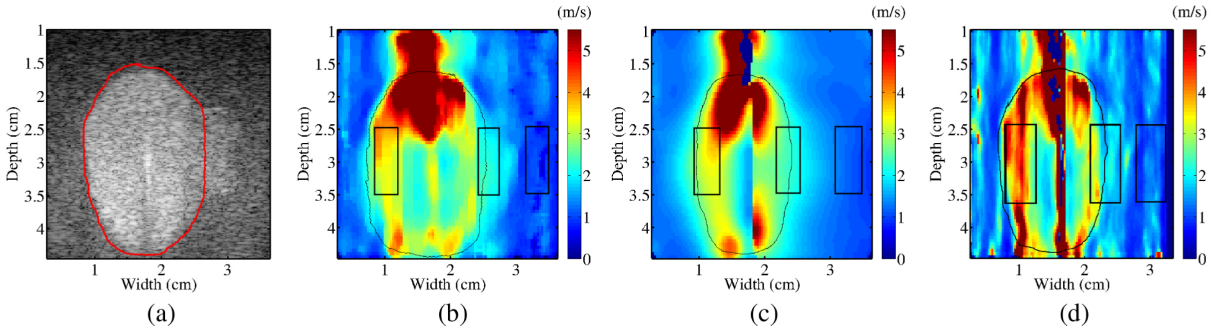

FIG. 8. ROIs and inclusion boundaries used for Phantom-1 are shown. Boundary used for B-mode area estimation is shown in (a). Boundaries for area estimation and ROIs used for calculating various statistics on the SWV maps are shown in (b), (c), and (d).

previously in Sec. 3.C. In order to gauge the performance of the particle filtering algorithm vis-a-vis existing imaging and data processing techniques, SWV estimates were obtained from two other methods. In the first method, a simple least-squares fourth order polynomial fit was used to filter the raw TTP data. Young's modulus was calculated using Eq. (1). SWV and shear modulus estimates obtained from these four different methods (EVE with particle filtering, EVE with least-squares filtering, SSI, and mechanical testing) are summarized in Tables I and II. Image quality metrics were calculated for the SWV maps obtained using the three different filtering algorithms. These are shown in Table III. Standard deviations are calculated from individual SNR, C, and CNR values in decibel obtained from each of the ten datasets. Sample outlines are shown in Figs. 8 and 9. Area estimate results are summarized in Table IV.

Results of EVE and B-mode scans of the two phantoms are shown in Figs. 8 and 9. Observe that in the SWV reconstruction, the irregular tumor area can be distinguished from the stiff inclusion and the background material. For comparison, the SWV images generated using a simple least-squares fourth order polynomial fitting method and using a moving average filter area are also shown. Although there is greater noise reduction and smoothing in the least-squares fit, the boundary details of the inclusion and partially ablated region get smeared out. For comparison, SWV maps obtained using the SSI technique are also shown in Fig. 10.

5. DISCUSSION

Observe from Fig. 8 that the particle filtering method applies an optimal amount of smoothing to the raw TTP data and produces good boundary delineation even between the inclusion and the irregular tumor regions that do not differ greatly in their shear modulus values. There is always a risk of over or undersmoothing when using *ad hoc* function fitting algorithms (like least-squares) that may blur boundary details. Quantitative estimates of SWVs and Young's moduli obtained using the particle filter agree well with the ground truth obtained from mechanical testing and least-squares filtering.

The SNR, C, and CNR values indicate that the particle filter is within a few decibel of the least-squares technique in suppressing noise, while providing better visual delineation between stiffer and softer areas in the phantom. The particle filtered SWV maps have quite high SNR and CNR values of at least 30 and 40 dB, respectively. These test metrics do not account for any measurement bias that may be present in the raw TTP data and are used only to compare the performance of the two filtering methods.

Finally, inclusion area estimates obtained from the particle filtered SWV maps are quite close to those obtained from B-mode imaging. As seen from Table IV, the least-squares method underestimates the inclusion size which may be a side effect of oversmoothing. It is worth noting that the contrast between the three different regions of the phantom easily visible

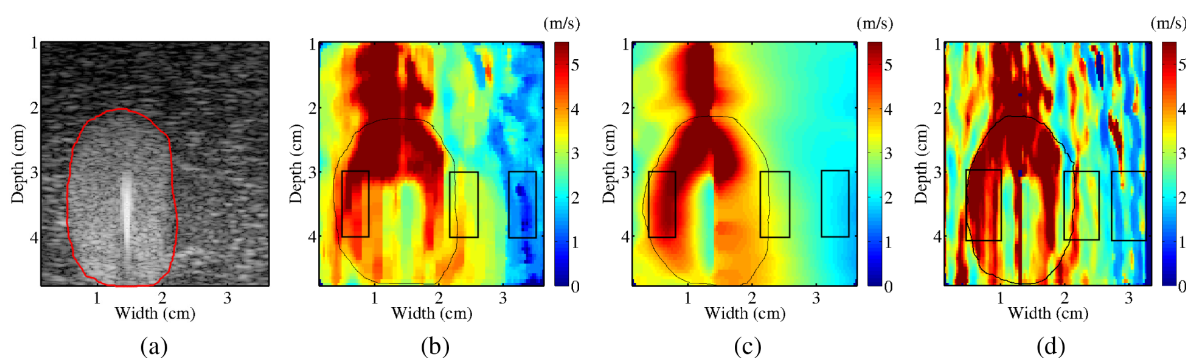

FIG. 9. ROIs and inclusion boundaries used for Phantom-2 are shown. Boundary used for B-mode area estimation is shown in (a). Boundaries for area estimation and ROIs used for calculating various statistics on the SWV maps are shown in (b), (c), and (d).

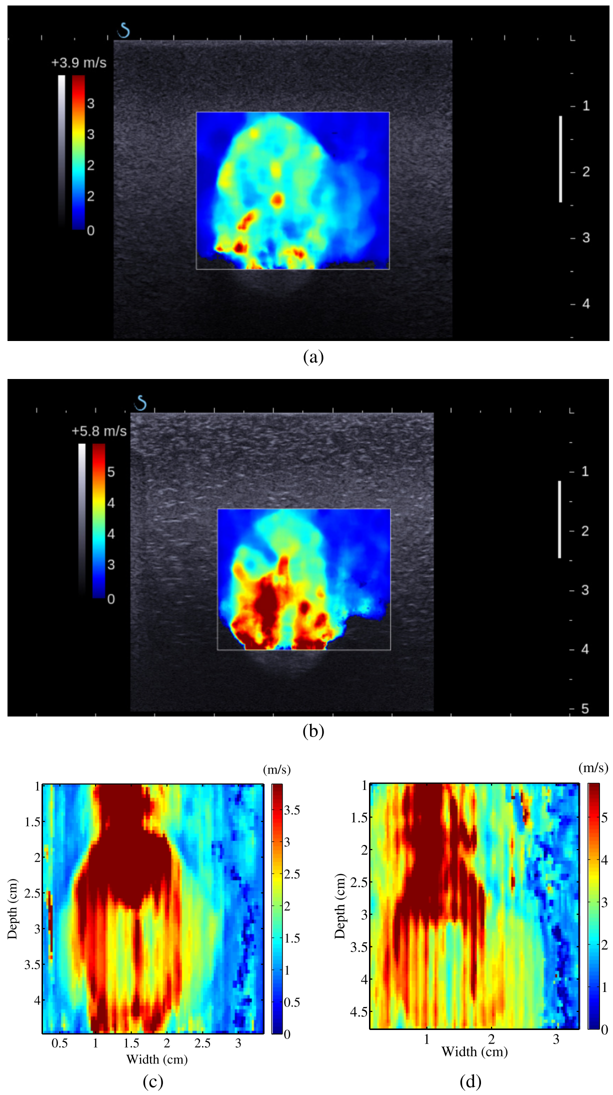

FIG. 10. SWV maps obtained using the clinical software interface of the Supersonic Imagine Aixplorer scanner using SSI are shown. Results from Phantom-1 and Phantom-2 are shown in (a) and (b), respectively. Reconstructions using the particle filtering algorithm are shown again on the same SWV scale for comparison in (c) and (d).

in B-mode is because of intentionally increased backscatter contrast in these manufactured phantom materials. In real tissue, differentiating stiffer and softer areas using B-mode scans is often challenging due to mixed echogenic contrast.[33] Area estimates may be susceptible to user variability because of the manual outlining step. Therefore, these measurements should not be used as the primary metric for comparing the performance of these SWV image reconstruction algorithms.

Young's modulus estimates of the stiffer areas in Phantom-1 that are obtained from mechanical testing do not agree with the results from ultrasound elastography estimates obtained from EVE and SSI. There is much better agreement of modulus estimates for the data obtained from Phantom-2. This may be because Phantom-1 is over a year old and there is a possibility of gradual degradation of the stiffness of phantom materials over time.[34] Cylindrical samples that used in mechanical testing are stored separately and hence are not under identical physical conditions as the material in the actual phantom. Moreover, the numbers obtained from elastography may have an inherent bias because the raw data undergo multiple smoothing and filtering operations before obtaining these modulus estimates.

SWV maps obtained using the Supersonic Imagine scanner are shown in Fig. 10. It is apparent from these images that EVE has the ability of generating SWV maps at greater depths and larger fields of view. Due to imaging depth limitations, inclusion area estimates could not be obtained using SSI. The proprietary velocity reconstruction algorithm appears to use a greater degree of smoothing. SWV estimates appear lower than those obtained with the particle filter. Nevertheless, the SSI technique differentiates various regions in the phantoms quite well, especially in case of Phantom-1 as seen in Fig. 10(a).

The ability of EVE technique to resolve fine boundary details is limited by the shear wave pulse width used. The data shown in this paper were generated using a 30 ms wide shear wave pulse. Although it may be possible to obtain sharper delineation by using a narrower pulse, it was observed during experimentation that due to certain physical limitations of the actuator system, accurate amplitude control could not be obtained for shorter vibration durations. The effect of the width of the pulse on estimation of TTP values and subsequent effect on the resolution of the SWV images will be analyzed in the future.

The data processing algorithm used in this paper assume that there is pure lateral propagation of the wave throughout the phantom. This assumption fails to hold for regions above and below the inclusion because the needle is bonded only to the interior of the inclusion.[35] As a result, SWV artifacts can be seen in the regions that are shallower or deeper than the stiffer ellipsoid. In order to focus attention on the data obtained from the regions that are laterally adjacent to area where the needle is bound to the phantom material, the SWV maps in Figs. 8 and 9 are shown beginning at a depth of about 1 cm. The wave propagation phenomenon above and below the stiff ellipsoid is more complex than pure transverse wave motion and a separate study to analyze this aspect may be necessary.

The data acquisition system is capable of operating at a frame rate of about 2 kHz which provides sufficient time sampling to track the shear wave pulse. As a practical matter, the particle filter runs slower than least-squares polynomial fitting. However, the algorithm is parallelizable because data at each depth are filtered independently. The current test implementation takes a few minutes to reconstruct each image. It is quite common to see a speedup by an order of magnitude when implemented as compiled code, providing almost real-time monitoring capability.

6. CONCLUSION

This paper presented a model-based denoising scheme that reduces the risk of oversmoothing SWV maps and produces visually appealing delineation results. Results from simulated data show that the particle filter is less susceptible to noise than a sliding window averaging filter. Test metrics calculated using experimental phantom data show that the proposed filtering method does equally well as least-squares filtering without smearing out the change points and providing a clear visual distinction between various stiffness regions in the phantom.

ACKNOWLEDGMENTS

The authors would like to thank Ryan DeWall (Department of Medical Physics, University of Wisconsin-Madison) for assistance with the data acquisition system and finite element simulation model; Professor James Bucklew and Professor William Sethares (Department of Electrical and Computer Engineering, University of Wisconsin–Madison) for discussions about the stochastic model and practical implementation issues with the particle filter algorithm. This work was supported in part by NIH-NCI Grant Nos. R01CA112192-S103 and R01CA112192-05.

APPENDIX: PARTICLE FILTER ALGORITHM

This section presents the details of the particle filter algorithm. The complete algorithm is a combination of existing algorithms presented in the papers by Arulampalam *et al.*[19] and Doucet *et al.*[24]

Input: $Y_{1:N}$: noisy data vector of length N

N_s: number of particles to use

N_T: threshold for resampling

σ^2: Gaussian noise variance

p: probability of staying in the same slope value

$[LB, UB]$: lower and upper bounds for slope values

Output: $M_{1:N}$: optimal state sequence

procedure ParticleSmoother($\{Y_k\}_{k=1}^{N}, N_s, N_T, p, \sigma^2, [LB, UB]$)
  for $k = 1 : N$ **do**
    for $i = 1 : N_s$ **do**
      Randomly draw $M_k^i \sim p(M_k^i | M_{k-1}^i)$ Eq. (5)
      Update weight ω_k^i using Eq. (8) for each $i = 1 : N_s$
    end for
    Normalize all weights $\omega_k^i \leftarrow \omega_k^i / \sum_{i=1}^{N_s} \omega_k^i$
    Calculate effective sample size $N_{eff} \leftarrow \frac{1}{\sum_{i=1}^{N_s} (\omega_k^i)^2}$.
    if $N_{eff} < N_T$ **then**
      Calculate covariance matrix $S_k \leftarrow cov(M_k^i, \omega_k^i)$ and Cholesky factorization $D_k D_k^T = S_k$
      $\{M_k^i, \omega_k^i\}_{i=1}^{N_s} \leftarrow$ Resample($\{M_k^i, \omega_k^i\}_{i=1}^{N_s}$)
      for $j = 1 : N_s$ **do**
        Draw $\epsilon^i \sim$ Epanechnikov Kernel
        $M_k^i \leftarrow M_k^i + D_k \epsilon^i$
      end for
    end if
  end for
  $\{\omega_k^i\}_{i=1}^{N_s} \leftarrow$ BackwardSmooth($\{M_k^i, \omega_k^i\}_{i=1}^{N_s}$)
  for $k = 1 : N$ **do**
    Calculate optimal state $M_k \leftarrow \sum_{i=1}^{N_s} \omega_k^i M_k^i$ by Eq. (9).
  end for
end procedure

FIG. 11. Details of the particle filter algorithm in pseudocode adapted from Algorithm 6 in the paper by Arulampalam *et al.* (Ref. 19) and Section V of Doucet *et al.* (Ref. 24).

```
Input: {M_k^i, ω_k^i}: set of particles and weights
Output: {M_k^i, ω_k^i}: updated set of particles and weights
procedure RESAMPLE({M_k^i, ω_k^i})
    Initialize cumulative distribution function c_1 ← 0
    for i = 2 : N_s do
        c_i ← c_{i−1} + w_k^i
    end for
    Draw u_1 uniformly randomly from [0, 1/N_s]
    for i = 1 : N_s do
        u_i ← u_1 + (i − 1)/N_s
        while u_i > c_j do
            j ← j + 1
        end while
        M_k^i ← M_k^j
        ω_k^i ← 1/N_s
    end for
end procedure
```

FIG. 12. Resampling algorithm used within the particle filter algorithm shown in Fig. 11.

```
Input: {M_k^i, ω_k^i}_{i=1}^{N_s}: set of particles and weights
Output: {ω_k^i}_{i=1}^{N_s}: set of backward smoothed weights
procedure BACKWARDSMOOTH({M_k^i, ω_k^i}_{i=1}^{N_s})
    for k = N − 1 : 1 do
        for i = 1 : N_s do
            Recalculate ω_k^i ← Σ_{j=1}^{N_s} ω_{k+1}^j · ω_k^i p(M_{k+1}^j | M_k^i) / Σ_{l=1}^{N_s} ω_k^l p(M_{k+1}^j | M_k^l)
        end for
    end for
end procedure
```

FIG. 13. Backward smoothing routine used in the particle filter algorithm shown in Fig. 11.

[a]Electronic mail: ingle@wisc.edu
[b]Electronic mail: ma.chi@mayo.edu
Q5 [c]Current address: Medical Physics Resident at Mayo Clinic, Rochester, Minnesota ■.
[d]Electronic mail: tvarghese@wisc.edu

[1]A. Sarvazyan, O. Rudenko, S. Swanson, J. B. Fowlkes, and S. Emelianov, "Shear wave elasticity imaging: A new ultrasonic technology of medical diagnostics," Ultrasound Med. Biol. **24**(9), 1419–1435 (1998).
[2]M. Palmeri, M. Wang, J. Dahl, K. Frinkley, and K. Nightingale, "Quantifying hepatic shear modulus *in vivo* using acoustic radiation force," Ultrasound Med. Biol. **34**(4), 546–558 (2008).
[3]L. Sandrin, M. Tanter, S. Catheline, and M. Fink, "Shear modulus imaging with 2-D transient elastography," IEEE Trans. Ultrason., Ferroelectr., Freq. Control **49**(4), 426–435 (2002).
[4]L. Sandrin, M. Tanter, J. Gennisson, S. Catheline, and M. Fink, "Shear elasticity probe for soft tissues with 1-D transient elastography," IEEE Trans. Ultrason., Ferroelectr., Freq. Control **49**(4), 436–446 (2002).
[5]S. Bharat and T. Varghese, "Radiofrequency electrode vibration-induced shear wave imaging for tissue modulus estimation: A simulation study (L)," J. Acoust. Soc. Am. **128**(4), 1582–1585 (2010).
[6]R. DeWall and T. Varghese, "Shear wave velocity imaging using transient electrode perturbation: Phantom and *ex vivo* validation," IEEE Trans. Med. Imaging **30**(3), 666–678 (2011).
[7]K. Nightingale, S. McAleavey, and G. Trahey, "Shear-wave generation using acoustic radiation force: *In vivo* and *ex vivo* results," Ultrasound Med. Biol. **29**(12), 1715–1723 (2003).
[8]M. Wang, M. Palmeri, V. Rotemberg, N. Rouze, and K. Nightingale, "Improving the robustness of time-of-flight based shear wave speed reconstruction methods using RANSAC in human liver *in-vivo*," Ultrasound Med. Biol. **36**(5), 802–813 (2010).
[9]Y. Zheng, S. Chen, W. Tan, R. Kinnick, and J. Greenleaf, "Detection of tissue harmonic motion induced by ultrasonic radiation force using pulse-echo ultrasound and Kalman filter," IEEE Trans. Ultrason., Ferroelectr., Freq. Control **54**(2), 290–300 (2007).
[10]J. McLaughlin and D. Renzi, "Shear wave speed recovery in transient elastography and supersonic imaging using propagating fronts," Inverse Probl. **22**(2), 681–706 (2006).
[11]M. Tanter, J. Bercoff, A. Athanasiou, T. Deffieux, J.-L. Gennisson, G. Montaldo, M. Muller, A. Tardivon, and M. Fink, "Quantitative assessment of breast lesion viscoelasticity: Initial clinical results using supersonic shear imaging," Ultrasound Med. Biol. **34**(9), 1373–1386 (2008).
[12]J. Klein, J. McLaughlin, and D. Renzi, "Improving arrival time identification in transient elastography," Phys. Med. Biol. **57**(8), 2151–2168 (2012).
[13]N. Rouze, M. Wang, M. Palmeri, and K. Nightingale, "Robust estimation of time-of-flight shear wave speed using a radon sum transformation," IEEE Trans. Ultrason., Ferroelectr., Freq. Control **57**(12), 2662–2670 (2010).
[14]H. Zhao, P. Song, M. Urban, R. Kinnick, M. Yin, J. Greenleaf, and S. Chen, "Bias observed in time-of-flight shear wave speed measurements using radiation force of a focused ultrasound beam," Ultrasound Med. Biol. **37**(11), 1884–1892 (2011).
[15]T. Deffieux, J. Gennisson, B. Larrat, M. Fink, and M. Tanter, "The variance of quantitative estimates in shear wave imaging: Theory and experiments," IEEE Trans. Ultrason., Ferroelectr., Freq. Control **59**(11), 2390–2410 (2012).
[16]B. Banerjee, D. Roy, and R. Vasu, "Efficient implementations of a pseudo-dynamical stochastic filtering strategy for static elastography," Med. Phys. **36**, 3470–3476 (2009).
[17]T. Marchant, A. Skalski, and B. Matuszewski, "Automatic tracking of implanted fiducial markers in cone beam CT projection images," Med. Phys. **39**(3), 1322–1334 (2012).
[18]T. Raveendran, S. Gupta, R. Vasu, and D. Roy, "A pseudo-time EnKF incorporating shape based reconstruction for diffuse optical tomography," Med. Phys. **39**, 1092–1101 (2012). Q6
[19]M. S. Arulampalam, S. Maskell, N. Gordon, and T. Clapp, "A tutorial on particle filters for online nonlinear/non-Gaussian Bayesian tracking," IEEE Trans. Signal Process. **50**(2), 174–188 (2002).
[20]W. Gilks and C. Berzuini, "Following a moving target—Monte Carlo inference for dynamic Bayesian models," J. R. Stat. Soc.: Ser. B (Stat. Methodol.) **63**(1), 127–146 (2001).
[21]N. Bergman, A. Doucet, and N. Gordon, "Optimal estimation and Cramer-Rao bounds for partial non-Gaussian state space models," Ann. Inst. Stat. Math. **53**(1), 97–112 (2001).
[22]C. Musso, N. Oudjane, and F. LeGland, "Improving regularized particle filters," in *Sequential Monte Carlo Methods in Practice* (Springer-Verlag, New York, NY, 2001), pp. 247–271.
[23]V. Epanechnikov, "Non-parametric estimation of a multivariate probability density," Theory Probab. Its Appl. **14**(1), 153–158 (1969).
[24]A. Doucet, S. Godsill, and C. Andrieu, "On sequential Monte Carlo sampling methods for Bayesian filtering," Stat. Comput. **10**(3), 197–208 (2000).
[25]S. Bharat, T. Varghese, E. Madsen, and J. Zagzebski, "Radiofrequency ablation electrode displacement elastography: A phantom study," Med. Phys. **35**(6), 2432–2442 (2008).
[26]E. Madsen, G. Frank, T. Krouskop, T. Varghese, F. Kallel, and J. Ophir, "Tissue-mimicking oil-in-gelatin dispersions for use in heterogeneous elastography phantoms," Ultrason. Imaging **25**(1), 17–38 (2003).
[27]A. Athanasiou, A. Tardivon, M. Tanter, B. Sigal-Zafrani, J. Bercoff, T. Deffieux, J. Gennisson, M. Fink, and S. Neuenschwander, "Breast lesions: Quantitative elastography with supersonic shear imaging–preliminary results," Radiology **256**(1), 297–303 (2010).
[28]T. Varghese and J. Ophir, "Performance optimization in elastography: Mul-

ticompression with temporal stretching," Ultrason. Imaging **18**(3), 193–214 (1996).

[29]T. Deffieux, J.-L. Gennisson, J. Bercoff, and M. Tanter, "On the effects of reflected waves in transient shear wave elastography," IEEE Trans. Ultrason., Ferroelectr., Freq. Control **58**(10), 2032–2035 (2011).

[30]P. Song, H. Zhao, A. Manduca, M. Urban, J. Greenleaf, and S. Chen, "Comb-push ultrasound shear elastography (CUSE): A novel method for two-dimensional shear elasticity imaging of soft tissues," IEEE Trans. Med. Imaging **31**(9), 1821–1832 (2012).

[31]T. Varghese and J. Ophir, "A theoretical framework for performance characterization of elastography: The strain filter," IEEE Trans. Ultrason., Ferroelectr., Freq. Control **44**(1), 164–172 (1997).

[32]T. Varghese and J. Ophir, "An analysis of elastographic contrast to noise ratio," Ultrasound Med. Biol. **24**(6), 915–924 (1998).

[33]T. Varghese, "Quasi-static ultrasound elastography," Ultrasound Clin. **4**(3), 323–338 (2009).

[34]E. Madsen, M. Hobson, H. Shi, T. Varghese, and G. Frank, "Stability of heterogeneous elastography phantoms made from oil dispersions in aqueous gels," Ultrasound Med. Biol. **32**(2), 261–270 (2006).

[35]R. DeWall and T. Varghese, "Improving thermal ablation delineation with electrode vibration elastography using a bidirectional wave propagation assumption," IEEE Trans. Ultrason., Ferroelectr., Freq. Control **59**(1), 168–173 (2012).